Identifiability of 3D Attributed Scattering Features from Sparse Nonlinear Apertures

Julie Ann Jackson and Randolph L. Moses

Ohio State University, Dept. of Electrical and Computer Engineering, Columbus, OH, USA

ABSTRACT

Attributed scattering feature models have shown potential in aiding automatic target recognition and scene visualization from radar scattering measurements. Attributed scattering features capture physical scattering geometry, including the non-isotropic response of target scattering over wide angles, that is not discerned from traditional point scatter models. In this paper, we study the identifiability of canonical scattering primitives from complex phase history data collected over sparse nonlinear apertures that have both azimuth and elevation diversity. We study six canonical shapes: a flat plate, dihedral, trihedral, cylinder, top-hat, and sphere, and three flight path scenarios: a monostatic linear path, a monostatic nonlinear path, and a bistatic case with a fixed transmitter and a nonlinear receiver flight path. We modify existing scattering models to account for nonzero object radius and to scale peak scattering intensities to equate to radar cross section. Similarities in some canonical scattering responses lead to confusion among multiple shapes when considering only model fit errors. We present additional model discriminators including polarization consistency between the model and the observed feature and consistency of estimated object size with radar cross section. We demonstrate that flight path diversity and combinations of model discriminators increases identifiability of canonical shapes.

Keywords: SAR, parametric scattering, sparse aperture, nonlinear flight path, feature extraction, ATR

1. INTRODUCTION

Attributed scattering feature models have shown potential in aiding automatic target recognition and scene visualization from radar scattering measurements.[1–5] Attributed scattering features capture physical scattering geometry, including the limited response of target scattering over wide angles, that is not discerned from traditional point scatter models. Development of algorithms for estimating attributed features from SAR data support the need for accurate target recognition algorithms in difficult environments, such as urban areas. A number of collection geometries are currently being considered to address needs of persistent surveillance and surveillance to support urban operations. We present recent results on feature identifiability from sparse collection apertures that support these surveillance needs.

Three-dimensional SAR images require data diversity in frequency, azimuth, and elevation and are typically created from multiple passes of the radar platform at several closely-spaced elevations (see Figure 1(a)). However, multi-pass data collection can be costly in terms of collection time and data storage/processing. Previously, we demonstrated a three-dimensional feature extraction method using interferometric SAR (IFSAR), with data collected along a linear sampling of azimuth angles at two closely-spaced elevations.[5] Specifically, we classified canonical scattering features using fully-polarimetric data and estimated scattering feature locations, dimensions, and orientations using a combination of nonlinear least-squares fit and IFSAR phase processing; however, not all three-dimensional information was identifiable from this aperture pair due to a lack of aspect diversity. Also, fully-polarimetric data is not always collected and so may not be a practical solution to feature classification. It is desirable to ascertain three-dimensional scene information from a single-pass, sparse nonlinear aperture (some subset of the data spanned by the multi-pass collection), such as, for example, the arbitrary path depicted in Figure 1(b). In this paper, we study the ability to accurately identify individual features from sparse apertures. The results provide a baseline comparison for future work in joint classification of multiple scattering features. We demonstrate that aspect diversity increases identifiability of a set of canonical scattering features but additional information is needed for a robust classification scheme. Previous works[5–10] have shown that fully-polarimetric data leads to correct classification of features when coupled with additional information about the persistence of the scatterer. We show that polarization estimates of even or odd bounce scattering reduces feature confusion

among the best-fit model features. We also present a model discriminator that may be used for single or multiple polarization channels and which checks the consistency of the estimated object size with its radar cross section.

The set of canonical scattering features used in this paper include a flat plate, dihedral, trihedral, cylinder, top-hat, and sphere. Bistatic parametric scattering models for these features were proposed by Rigling;[4,11] we have updated the models and present them in Section 2. In Section 3 we present three model discriminators and feature identification results for three flight path scenarios. We demonstrate that flight path diversity and combinations of the model discriminators increases identifiability of the canonical shape features.
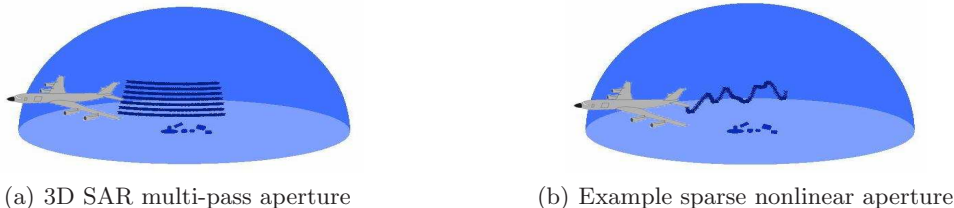

(a) 3D SAR multi-pass aperture   (b) Example sparse nonlinear aperture

Figure 1. Depiction of sampling a SAR aperture for 3D image formation with (a) a multi-pass collection and (b) an example sparse nonlinear aperture with azimuth and elevation diversity.

2. 3D ATTRIBUTED SCATTERING MODELS

Under a high-frequency assumption, scattering from complex objects may be modeled as the sum of responses from individual scatterers. The received radar signal from bistatic scattering of an individual canonical feature of type m may be represented as[1]

$$S_m(k, \theta_t, \phi_t, \theta_r, \phi_r; \vec{\Theta}_m) = M_m(k, \theta_t, \phi_t, \theta_r, \phi_r; \vec{\Theta}_m)e^{jk\Delta R(\vec{\Theta}_m)} \tag{1}$$

where the angles (ϕ_t, θ_t) describe the radar transmitter location in azimuth and elevation and the angles (ϕ_r, θ_r) describe the receiver azimuth and elevation location. The frequency dependence of the scatterer response is given by the wavenumber, $k = \frac{2\pi f}{c}$. The vector $\vec{\Theta}_m$ contains parameters corresponding to a reflector of type m, including its complex polarization response $A \triangleq A_r + jA_i$, its (X, Y, Z) location, its orientation (roll $\tilde{\psi}$, pitch $\tilde{\theta}$, and yaw $\tilde{\phi}$), and its applicable size dimensions (length L, height H, and radius r). We consider six primitive scattering types, described below. Due to symmetries in some cases, not all scattering types have the same parameters, or the same number of parameters, in the vector $\vec{\Theta}_m$. The term $\Delta R(\vec{\Theta}_m)$ describes the location of the object relative to scene center; we assume that the transmit and receive radar platforms are in the far-field so that $\Delta R(\vec{\Theta}_m)$ may be approximated by the bistatic differential range[11]

$$\Delta R \approx X(\cos\theta_t \cos\phi_t + \cos\theta_r \cos\phi_r) + Y(\cos\theta_t \sin\phi_t + \cos\theta_r \sin\phi_r) + Z(\sin\theta_t + \sin\theta_r), \tag{2}$$

where (X, Y, Z) are the Cartesian coordinates of a reference point on the object. Our location reference points correspond to the origin of the axes drawn in Figure 2 for each shape.

Rigling has proposed 3D bistatic parametric scattering models for six canonical shapes based on the geometric theory of diffraction (GTD).[4,11] The shapes, which include a flat plate, dihedral, trihedral, cylinder, top-hat, and sphere, are depicted in Figure 2. The three-dimensional scattering models are the separable product of two-dimensional scattering responses, coupled with rotations of the responses to model arbitrary object orientation. Specifically, the models are comprised of products of three basic 2D scattering mechanisms – a circle, a right-angle, and a flat plate. For example, a vertically-oriented top-hat is modeled as having a circular shape (isotropic variation) in azimuth and right-angle shape in elevation; therefore, the 3D top-hat model is given as a product of circular and right-angle scattering models. For general orientation, this separable response is rotated so that the final model is a non-separable response, mixing the two components.

Rigling's models considered a point phase center model and normalized amplitude scaling for each object. Below, we extend Rigling's models to include amplitude scaling so that the peak scattering intensity is equal to
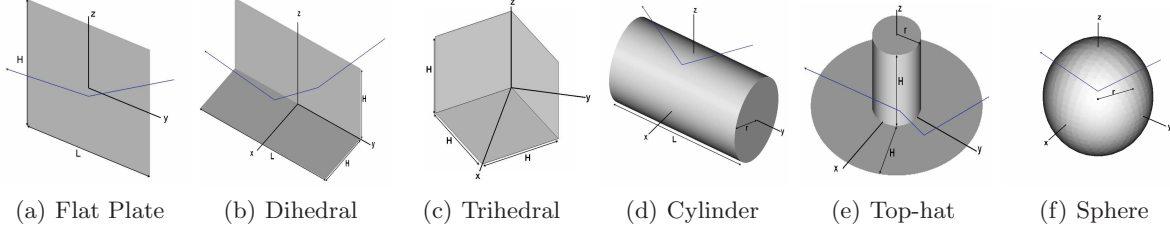
Figure 2. Canonical scattering primitives.

the object's peak radar cross section. We adopt Rigling's point phase center model for three of the canonical shapes (plate, dihedral, and trihedral) and extend his models of the cylinder, top-hat, and sphere to include phase terms that account for the nonzero radius of these objects.

2.1. Plate

The scattering response from a flat rectangular plate is characterized by sinc responses along its length L and height H dimensions and is given by

$$M_{\text{plate}}(\vec{\Theta}_{plate} = [A, X, Y, Z, \tilde{\psi}=0, \tilde{\theta}=0, \tilde{\phi}=0, L, H]) = \frac{-jk}{\sqrt{\pi}} A \operatorname{sinc}\left[k\frac{L}{2}(\sin\phi_t \cos\theta_t + \sin\phi_r \cos\theta_r)\right]$$

$$\times \operatorname{sinc}\left[k\frac{H}{2}(\sin\theta_t + \sin\theta_r)\right], \qquad \theta_t, \theta_r \in \left[-\frac{\pi}{2}, \frac{\pi}{2}\right] \quad \phi_t, \phi_r \in \left[-\frac{\pi}{2}, \frac{\pi}{2}\right] \qquad (3)$$

where $A = LH$.

2.2. Dihedral

The scattering response from a dihedral is characterized by a flat plate response along its length L and a right angle response dependent on the height H and depth, which we assume is also equal to H. The dihedral response is thus given by

$$M_{\text{dih}}(\vec{\Theta}_{dih} = [A, X, Y, Z, \tilde{\psi}=0, \tilde{\theta}=0, \tilde{\phi}=0, L, H]) = \frac{-jk}{\sqrt{\pi}} A \operatorname{sinc}\left[k\frac{L}{2}(\sin\phi_t \cos\theta_t + \sin\phi_r \cos\theta_r)\right]$$

$$\times \operatorname{sinc}\left[kH(\cos\theta_t - \cos\theta_r)\right] \sin\left(\frac{\theta_t + \theta_r}{2}\right), \qquad \theta_t, \theta_r \in \left[0, \frac{\pi}{4}\right] \quad \phi_t, \phi_r \in \left[\frac{-\pi}{2}, \frac{\pi}{2}\right] \qquad (4)$$

where $A = 2LH$. Note that in the monostatic case in which $\theta_t = \theta_r$, the second sinc function becomes constant and (4) becomes independent of H except in the amplitude term.

2.3. Trihedral

The trihedral scattering response is comprised of right-angle scattering responses along each dimension and is given by

$$M_{\text{tri}}(\vec{\Theta}_{tri} = [A, X, Y, Z, \tilde{\psi}=0, \tilde{\theta}=0, \tilde{\phi}=0, H]) = \frac{jk}{2\pi}\sqrt{72\pi} A \sin\left(\frac{\theta_t + \theta_r}{2}\right) \operatorname{sinc}\left[kH(\cos\theta_t - \cos\theta_r)\right]$$

$$\times \operatorname{sinc}\left[kH\left(\cos\left(\phi_r - \frac{\pi}{4}\right)\cos\theta_r - \cos\left(\phi_t - \frac{\pi}{4}\right)\cos\theta_t\right)\right] \begin{cases} \cos\left(\frac{\phi_t + \phi_r}{2} - \frac{\pi}{4}\right) & \phi_t, \phi_r \in \left[\frac{-\pi}{4}, 0\right] \\ -\sin\left(\frac{\phi_t + \phi_r}{2} - \frac{\pi}{4}\right) & \phi_t, \phi_r \in \left[0, \frac{\pi}{4}\right] \end{cases}, \quad \theta_t, \theta_r \in \left[0, \frac{\pi}{4}\right] \quad (5)$$

where $A = H^2$. Note that for the monostatic case ($\theta_t = \theta_r$ and $\phi_t = \phi_r$) both sinc responses becomes constant and the response in (5) is independent of the trihedral size H, except in the amplitude term.

2.4. Cylinder

The scattering response for a horizontal cylinder includes isotropic scattering about the elevation cut and plate-like scattering along the length dimension. The cylinder radius induces an offset in the apparent range location of the scatterer. The cylinder scattering response and range location are given by

$$M_{\text{cyl}}(\vec{\Theta}_{cyl} = [A, X, Y, Z, \tilde{\psi}=0, \tilde{\theta}=0, \tilde{\phi}=0, L, r]) = -\sqrt{\frac{jk}{\cos\phi_t}} A \cos\phi_r \, \text{sinc}\left[k\frac{L}{2}(\sin\phi_t + \sin\phi_r)\right]$$

$$\phi_t, \phi_r \in \left[-\frac{\pi}{2}, \frac{\pi}{2}\right] \tag{6}$$

$$\Delta R_{\text{cyl}} = \Delta R - \left(r\cos\left(\frac{\theta_t - \theta_r}{2}\right)(\cos\phi_t + \cos\phi_r)\right) \tag{7}$$

where $A = L\sqrt{r}$ in (6).

2.5. Top-hat

The scattering response for a vertically-oriented top-hat is characterized by isotropic scattering about the azimuth cut and right-angle scattering from the intersection of the cylindrical portion with the base. The apparent range location of the top-hat is offset from its location reference point by the cylinder radius. The top-hat scattering response and range location are given by

$$M_{\text{top}}(\vec{\Theta}_{top} = [A, X, Y, Z, \tilde{\psi}=0, \tilde{\theta}=0, \tilde{\phi}=0, H, r]) = -A\sqrt{jk\sqrt{2}\sin\left(\frac{\theta_t + \theta_r}{2}\right)}$$

$$\times \, \text{sinc}\left[2kH\sin\left(\frac{\theta_t + \theta_r}{2}\right)\sin\left(\frac{\theta_t - \theta_r}{2}\right)\right], \qquad \theta_t, \theta_r \in \left[0, \frac{\pi}{4}\right] \tag{8}$$

$$\Delta R_{\text{top}} = \Delta R - \left(r\cos\left(\frac{\phi_t - \phi_r}{2}\right)(\cos\theta_t + \cos\theta_r)\right) \tag{9}$$

where r is the cylinder radius and $A = H\sqrt{r}$ in (8). The right-angle response depends on the height H of the top-hat (which we assume is equal to the rim width), but for equal transmitter and receiver elevations H is not independent of the scattering amplitude.

2.6. Sphere

The sphere is an isotropic scatterer with constant amplitude response and apparent range offset by the sphere radius. The sphere scattering response and location are given by

$$M_{\text{sphere}}(\vec{\Theta}_{sphere} = [A, X, Y, Z, r]) = -\sqrt{\pi}A \tag{10}$$

$$\Delta R_{\text{sphere}} = \Delta R - \left(r(\cos\theta_t + \cos\theta_r)\cos\left(\frac{\phi_t - \phi_r}{2}\right)\cos\left(\frac{\theta_t + \theta_r}{2}\right) + r\sin\left(\frac{\theta_t + \theta_r}{2}\right)(\sin\theta_t + \sin\theta_r)\right) \tag{11}$$

where $A = r$ in (10). For monostatic SAR, the range offset in (11) reduces to $2r$–the two-way distance from the surface to the center of the sphere.

2.7. Rotated Scatterers

The above scattering model equations correspond to the bistatic SAR collection geometry and canonical shapes oriented as shown in Figure 2. Rigling[11] presents the rotation matrices required to obtain the scattering response for rotated scattering centers. For an object with roll $\tilde{\psi}$, pitch $\tilde{\theta}$, and yaw $\tilde{\phi}$, the effective transmitter and receiver look angles are

$$\left[\hat{\theta}_t, \hat{\phi}_t\right] = \left[\arctan\left(\frac{\hat{z}_t}{\sqrt{\hat{x}_t^2 + \hat{y}_t^2}}\right), \arctan\left(\frac{\hat{y}_t}{\hat{x}_t}\right)\right], \qquad \left[\hat{\theta}_r, \hat{\phi}_r\right] = \left[\arctan\left(\frac{\hat{z}_r}{\sqrt{\hat{x}_r^2 + \hat{y}_r^2}}\right), \arctan\left(\frac{\hat{y}_r}{\hat{x}_r}\right)\right] \quad (12)$$

where

$$\begin{bmatrix} \hat{x}_t \\ \hat{y}_t \\ \hat{z}_t \end{bmatrix} = \begin{bmatrix} \cos\tilde{\phi} & -\sin\tilde{\phi} & 0 \\ \sin\tilde{\phi} & \cos\tilde{\phi} & 0 \\ 0 & 0 & 1 \end{bmatrix} \begin{bmatrix} \cos\tilde{\theta} & 0 & -\sin\tilde{\theta} \\ 0 & 1 & 0 \\ \sin\tilde{\theta} & 0 & \cos\tilde{\theta} \end{bmatrix} \begin{bmatrix} 1 & 0 & 0 \\ 0 & \cos\tilde{\psi} & -\sin\tilde{\psi} \\ 0 & \sin\tilde{\psi} & \cos\tilde{\psi} \end{bmatrix} \begin{bmatrix} \cos\theta_t \cos\phi_t \\ \cos\theta_t \sin\phi_t \\ \sin\theta_t \end{bmatrix} \quad (13)$$

and the receiver positions are likewise defined. The rotated scattering responses are found by computing $M_m(k, \hat{\theta}_t, \hat{\phi}_t, \hat{\theta}_r, \hat{\phi}_r; \vec{\Theta}_m)$ from the above model equations.

2.8. Example Scattering Responses

In Figure 3, we show the monostatic scattering amplitudes of the canonical scatterers sampled over an aperture window covering $\phi \in [-10°, 10°]$ in azimuth and $\theta \in [20°, 40°]$ in elevation with frequency $f = 10\text{GHz}$. The size of each scatterer is listed in Table 1. The plate has pitch rotation $\tilde{\theta} = 30°$ so that the radar at elevation angle $\theta_{t,r} = 30°$ captures the specular response. The other scatterers are oriented as shown in Figure 2. On each amplitude response, we depict an example of linear and nonlinear SAR flight paths. Note that the observed radar return depends on the flight path which cuts through the scattering response; the constant elevation cuts for the plate, dihedral, and cylinder are easily confused. Increasing the monostatic radar aspect diversity helps to differentiate the scatterer types. However, in bistatic mode SAR aspect diversity is not as beneficial. In Figure 4 we show the bistatic scattering amplitudes of the canonical scatterers sampled over the same aperture as in the monostatic case, with the transmitter located at the center of the aperture window ($\phi_t = 0°, \theta_t = 30°$). We note that bistatic SAR will detect more specular responses than will monostatic SAR; however, in the bistatic case, all shapes but the sphere exhibit a sinc dependence along at least one dimension, leading to confusion between multiple shapes. In the next section, we explore the effects of aspect diversity via several flight path configurations and present methods for correctly identifying each scatterer shape.

3. SCATTERING PRIMITIVE IDENTIFIABILITY

Attributed scattering features are able to capture the physical geometry of scattering responses of a scene. In Section 2, we presented six 3D attributed feature models that, as shown in Figures 3 and 4, may have similar scattering responses, depending on the object size and orientation with respect to the SAR flight path. In this section, we study the ability to correctly identify each of the six canonical scattering shapes. We generate complex phase history observations of each canonical shape using Xpatch[12] electromagnetic scattering prediction software and compare them to the six parametric scattering models. Small mismatches between the parametric models and the Xpatch simulated responses are considered to be noise, so that model classification can be considered stochastically. Using thresholds on model fit error, polarization, and peak radar cross section we will characterize the ability to discriminate the true feature in three SAR flight path scenarios. We will demonstrate that flight path diversity and combined model discriminators decreases the number of confuser shapes, resulting in improved feature identification.

3.1. Observed Feature Simulation

We generate phase history (frequency domain) scattering responses for each of the canonical models using Xpatch electromagnetic scattering prediction software. Each shape is located at the origin. The plate has a pitch $\tilde{\theta} = 30°$; the other five shapes have roll, pitch, yaw orientations ($\tilde{\psi} = 0, \tilde{\theta} = 0, \tilde{\phi} = 0$) as depicted in Figure 2. The canonical shape dimensions are listed in Table 1. Complex phase history responses are computed
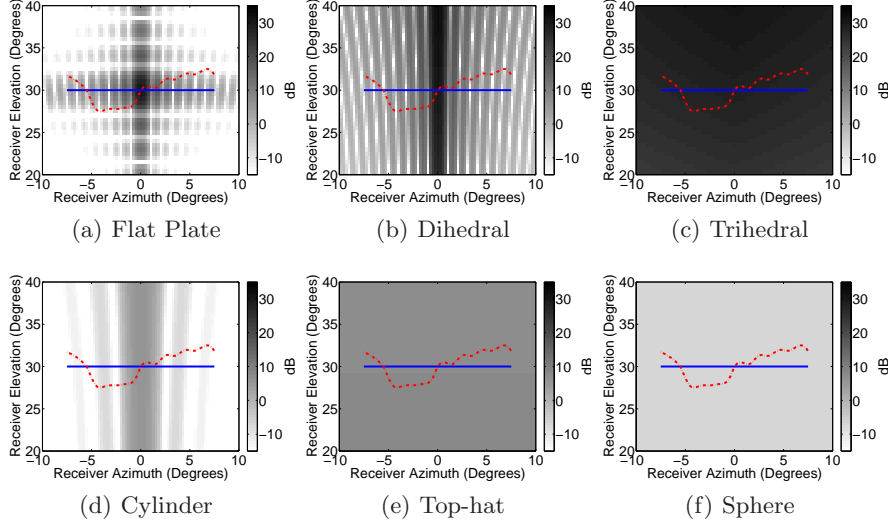
Figure 3. Monostatic scattering amplitude of canonical shapes over an aperture window $\phi \in [-10°, 10°], \theta \in [20°, 40°]$. The lines drawn through the middle of the aperture window represent example linear and nonlinear flight paths.

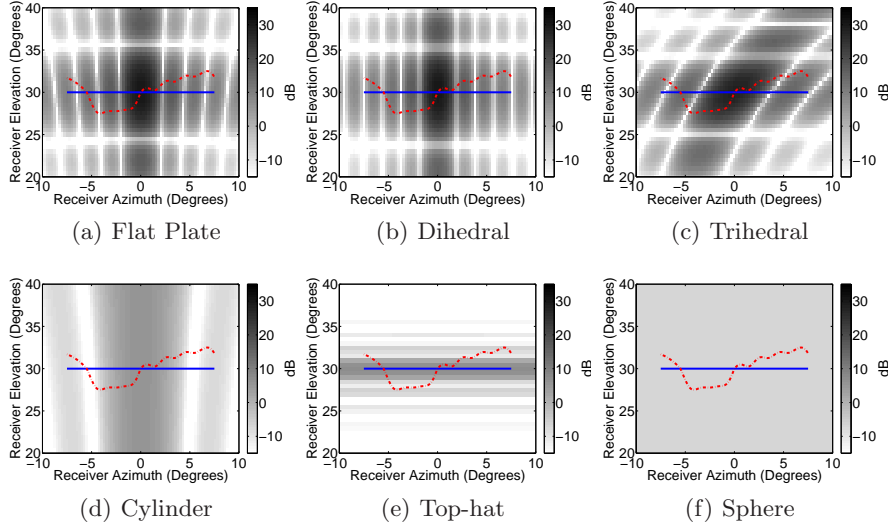**Figure 4.** Bistatic scattering amplitude of canonical shapes over an aperture window $\phi_r \in [-10°, 10°], \theta_r \in [20°, 40°]$, with transmitter positioned at $(\phi_t, \theta_t) = (0°, 30°)$. The lines drawn through the middle of the aperture window represent example linear and nonlinear receiver flight paths.

for three flight path configurations: (1) monostatic SAR with a linear flight path, (2) monostatic SAR with an arbitrary, nonlinear flight path and (3) bistatic SAR with a fixed transmitter and a receiver that follows the same nonlinear path as in the monostatic case (2). The receiver paths are plotted on the canonical shape amplitude responses in Figures 3 and 4. The linear path has $\theta_{t,r} = 30°$; the nonlinear path takes on arbitrarily-selected values in the window $\phi_r \in [-7.5°, 7.5°]$ and $\theta_r \in [27.5°, 32.5°]$ and passes through the center aperture point $(\phi_r, \theta_r) = (0°, 30°)$. For the bistatic case, the transmitter position is fixed at the center of the aperture window $(\phi_t, \theta_t) = (0°, 30°)$. For all flight paths, the bandwidth is 3.96 GHz and the radar center frequency is $f_c = 10.16$ GHz. Although we only consider object orientations that have one major axis parallel to the flight path, object rotations about the radar line of sight can be viewed as nonlinear flight paths. Thus, the arbitrary nonlinear flight path results are also representative of the feature classification results expected for rotated scatterers.

3.2. Model Fit

Noisy observations of each scatterer $Y_n = S_n + W$ may be produced by adding complex white Gaussian noise $W \sim \mathcal{CN}\left(0, \sigma^2\right)$ to the Xpatch-simulated scattering responses. Then, the nonlinear least-squares model fit for a scattering model of type m to observation Y_n of type n is

$$\hat{\Theta}_{m,n} = \arg \min_{\vec{\Theta}_m} \|Y_n - S_m(\vec{\Theta}_m)\|^2. \tag{14}$$

where the vector $\hat{\Theta}_m, n$ is an estimate of the test feature's scattering parameters. In this paper, we consider only the noiseless case, $\sigma = 0$, since confusion between scattering shapes may occur even in this best-case scenario. We numerically solve (14) for the best-fit parameters $\hat{\Theta}_{m,n}$ of each of the six shapes to each of the six feature observations Y_n, $m, n \in$ [plate, dihedral, trihedral, cylinder, top-hat, sphere].

In fitting the models to data, we treat A in each of the models as a separate, complex-valued amplitude that is not related to the other model parameters. We do so because in practice, radar measurements have amplitude uncertainty due to calibration errors, imperfect antenna corrections, etc. We therefore model the radar amplitudes separately, and later address, via radar cross section analysis, whether the amplitude terms are consistent with other parameter estimates. The latter consistency check can be carried out to within the expected amplitude precision of the radar system being considered.

Ideally, the feature model that corresponds to the true shape will have the minimum least-squares error. However, there is a small amount of mismatch between the Xpatch scattering predictions and the parametric scattering model responses, which we consider to be noise that corrupts the data. Therefore, the minimum fit error may not correspond to the true feature, since several of the models often well approximate the observed signal due to similarities in the scattering responses (e.g. sinc-like behavior due to finite object length), and the problem is treated stochastically. For Gaussian noise, the solution to the least-squares problem is the maximum likelihood (ML) estimator. The ML parameter estimates may be used in a generalized likelihood ratio test (GLRT) with thresholds set to classify features according to a desired false alarm rate. Therefore, we employ a GLRT-type classification scheme that accepts all models within a threshold τ_1 of the lowest fit error. Thus, the model fit classifier is

$$\hat{F}_n = \arg \left\{ \min_m \epsilon_{m,n} - \epsilon_{m,n} \right\} < \tau_1 \tag{15}$$

where $\epsilon_{m,n}$ is the fit error metric and $\hat{F}_n$ is a list of features that fit well to the observed data feature n. We scale the least-squares error to obtain the relative root mean squared error in dB so that for N complex phase history samples, $\epsilon_{m,n}$ becomes

$$\epsilon_{m,n} = 20 \log_{10} \sqrt{\frac{1}{2N} \frac{\|Y_n - S_m\|^2}{\|Y_n\|^2}}. \tag{16}$$

The model fit results are plotted in Figure 5 along with the observed feature signals. In Figure 5, there are six rows (one for each true shape) and three columns (one for each flight path scenario). For brevity, we show only the scattering signal amplitudes at the center frequency; however the nonlinear least squares model fits are performed using the complex phase history data over the entire 3.96 GHz bandwidth. Asterisks in the legends of Figure 5 denote the scattering responses whose plots are not visually distinguishable due to overlap with the observed feature signal. From Figure5, we note that in the monostatic constant elevation case the plate, dihedral, and cylinder all overlap, as expected from the similar sinc responses shown in Figure 3. The trihedral, top-hat, and sphere responses are all nearly constant and are easily approximated by all shapes by choosing short lengths which extend the mainlobe of their sinc responses to be nearly constant over the width of the aperture. Results are similar for the non-constant elevation case; however, asymmetry and lower sidelobe levels in the plate response distinguish it from the dihedral and cylinder. In the bistatic case, all model shapes except the sphere fit well to each observed shape, as expected from the scattering responses shown in Figure 4, due to the flexibility of the scattering models. The fit errors $\epsilon_{m,n}$ are tabulated in Tables 2, 4, and 6 for each of the flight path scenarios. The highlighted cells in each table indicate the model fits which are within $\tau_1 = 5$ dB of the best fit. As indicated by the plots in Figure 5, there are several instances when multiple scattering models fit

very well to the observed signal, indicating confusion between the target classes. In the next sections we present other model discriminators that improve classification performance.
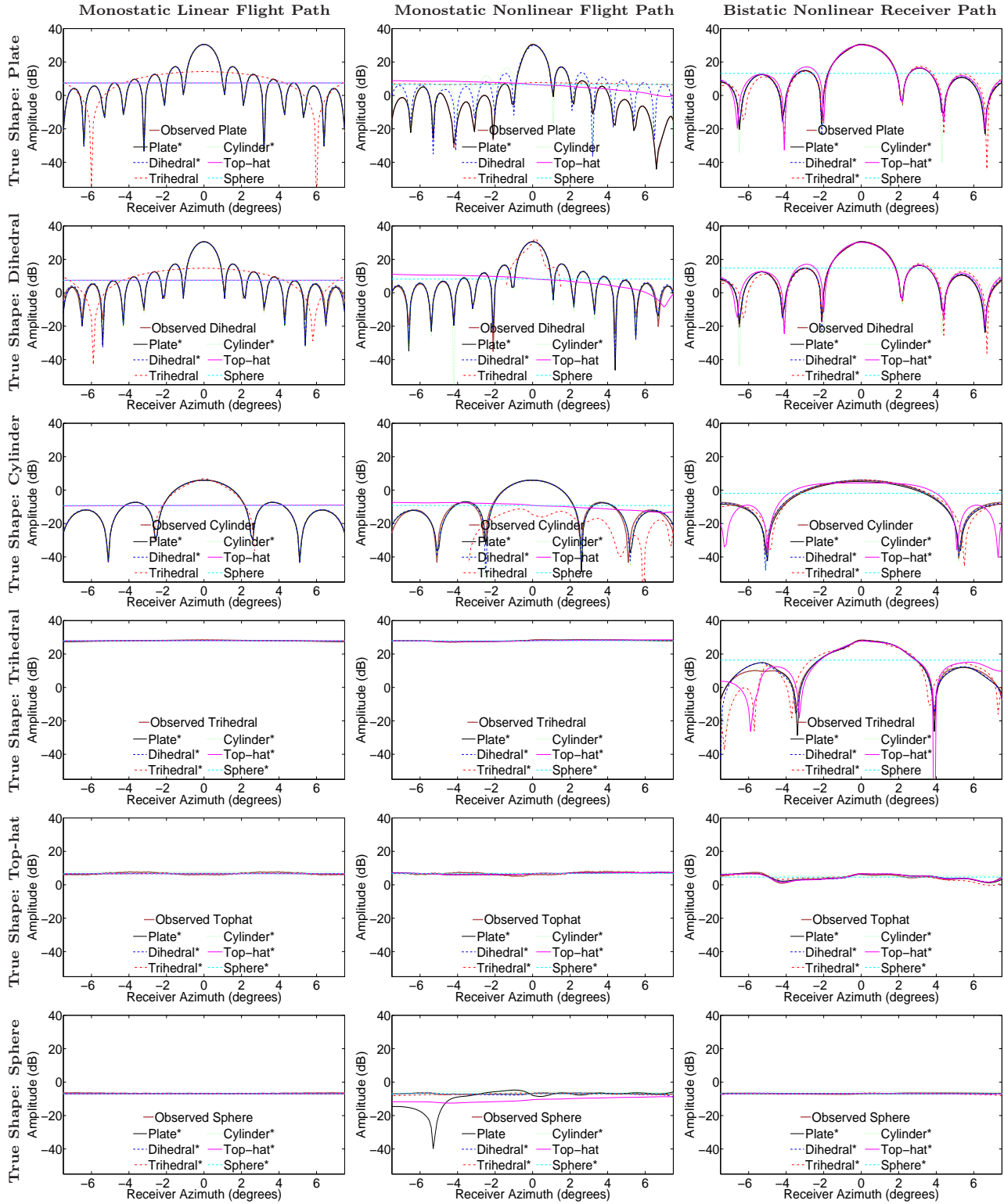

Figure 5. Xpatch simulated scattering responses of canonical shapes with best-fit models overlaid.

3.3. Radar Cross Section Consistency

Each of the scattering models in Section 2 defined a complex amplitude term $A = A_r + jA_i$ that, for a perfectly calibrated radar, is a real coefficient proportional to the effective area of the canonical shape. Radar cross section is related to effective area A_{eff} by[13] $\text{RCS} = \frac{4\pi A_{\text{eff}}^2}{\lambda^2}$. The peak radar cross section amplitudes for the canonical scatterers are found in the literature[13, 14] and are reproduced in Table 1. For the top-hat, we assume that the scattering from the shaft of the cylinder is dominant. Table 1 also lists the dimensions and corresponding radar cross sections for the shapes used in simulations for this paper. Note the large variation in the directivity of each shape results in a large range of radar cross sections for shapes of similar sizes. For example, for a sphere to have the same radar cross section as the 15 inch trihedral, the sphere would have a radius of approximately 66.8 feet. Thus, the radar cross section provides additional information about the true shape of the scattering feature. If the radar is sufficiently calibrated, the estimated radar cross section and the peak intensity of the scattering return will agree; otherwise, the estimated shape will not correspond to the true scattering feature. We show here that improved feature classification can be achieved by checking the consistency of the estimated object size with its peak radar cross section.

As in Section 3.2 we obtain parameter estimates for each canonical shape model fit to the observed data by solving (14). Next, we insert the dimension parameters estimated from (14) directly into the RCS equations listed in Table 1. Then, we compute the peak intensity response of the estimated scatterer. If the feature model corresponds to the observed feature, the RCS computation will agree with the peak scattering response. We discard features whose peak scattering intensity differs from the RCS by more than a threshold τ_2 that can be set to correspond to expected accuracies in the radar calibration. Therefore, the consistency check on estimated object size with its peak radar cross section may be written as

$$\hat{C}_{m,n} = \arg\left\{\left|\text{RCS}(\hat{\Theta}_{m,n}) - \max\|S_m(\hat{\Theta}_{m,n})\|^2\right| < \tau_2\right\} \tag{17}$$

where $\hat{C}_{m,n}$ is a list of features whose RCS estimate agrees with the observed scattering intensity. The peak intensity and dimension-based RCS estimates for each model-observation pair are listed in Table 3 for the constant elevation flight path case, Table 5 for the monostatic, non-constant elevation flight path, and Table 7 for the bistatic case. In each table, we highlight the cells included in the list $\hat{C}_{m,n}$ for a threshold $\tau_2 = 5$ dB. Cells that are not highlighted have an RCS inconsistency between the scattering intensity and the object size. As an example, let us consider the monostatic nonlinear flight path observation of dihedral scattering. The plate has low model fit error, with estimated length and height $L = 35.46''$, $H = 2.75''$, which yields an RCS estimate nearly 13dB below the peak scattering intensity. Therefore, the plate size and peak RCS are not consistent, and the plate is discarded as a possible match to the dihedral scatterer. We note that not all of the dimension parameters are estimable for all shapes; we include those cases in $\hat{C}_{m,n}$ as possible features since we cannot discard them on the basis of RCS inconsistency. Bistatic SAR mode allows us to estimate the height parameters for the dihedral, trihedral, and top-hat, and to compute the RCS mismatch, resulting in a reduced number of confused target features across the observation set. However, for our example, the plate, dihedral, and trihedral all have similar RCS amplitudes and are not distinguishable from RCS alone. Later, we will show that combining multiple model discriminators will reduce ambiguity between shapes. In the next section, we present a polarization-based method for discarding incorrect features.

Canonical Shape	Polarization Bounce	Peak RCS	Example Dimensions	Example RCS $\lambda = 2.95$ cm
Rectangular Plate	odd	$\frac{4\pi L^2 H^2}{\lambda^2}$	$L = 36$ in. $H = 12$ in.	1119.6 m^2
Dihedral	even	$\frac{8\pi L^2 H^2}{\lambda^2}$	$L = 36.0$ in. $H = 12$ in.	2239.2 m^2
Square Trihedral	odd	$\frac{12\pi H^4}{\lambda^2}$	$H = 15$ in.	1300.8 m^2
Cylinder	odd	$\frac{2\pi}{\lambda} r L^2$	$r = 5$ in. $L = 15$ in.	3.9 m^2
Top-hat	even	$\frac{2\pi r H^2}{\lambda}$	$r = 6$ in. $H = 18$ in.	6.8 m^2
Sphere	odd	πr^2	$r = 8$ in.	0.2 m^2

Table 1. Polarization bounce types and peak RCS values and corresponding dimensions for six canonical shapes.

3.4. Polarization Consistency

The feature classifications presented above use only a single channel of SAR phase history data. Fully-polarimetric data allows for classification of targets into odd-bounce and even-bounce scattering.[5, 9, 10] Thus, we can categorize the observed feature bounce using the methods listed by Jackson[5] and discard those models whose bounce type does not agree. The polarization bounce type for the six canonical shapes are listed in Table 1.

3.5. Combined Model Discriminators

In the previous sections, we presented three methods for identifying canonical scattering features. However, the individual model discriminators often included several potential shapes for each observed features. The polarization bounce estimate can only classify an observed feature as being even or odd bounce, which is not a unique characterization of the six canonical features. The RCS consistency check does not give unique feature classification results in the monostatic case due to the inestimable dimensions of some scattering features. Likewise, for data collection scenarios with limited aspect diversity, the model fit classifier does not provide a unique feature classification due to unobservable elevation dependencies of a particular feature type. For example, for a monostatic constant elevation flight path, the scattering dependence on elevation is constant and the plate, dihedral, and cylinder all have similar sinc-like responses due to their finite length. Therefore, we cannot achieve high probabilities of correct identification using the individual model fit, RCS, and polarization metrics. However, if we combine the information from two or more model discriminators, we reduce the number of confused shapes and show that nearly all of the features are identifiable.

Here, we introduce a structure for feature classification that incorporates information from multiple model discriminators. The best-fit models are computed for each observation. The resulting parameter estimates are used to compute multiple model discriminator outputs in parallel. Model classifier metrics may be inserted or deleted from the structure by inserting or deleting the corresponding branches in Figure 6. The lists of potential feature shapes from each branch are intersected to produce a final list of potential feature shapes. We combine the model fit classifier of Section 3.2 with (1) the RCS consistency check of Section 3.3, (2) the polarization bounce estimator of Section 3.4, and (3) both the RCS consistency check and polarization bounce estimator. The results are listed in Table 8 for the three flight path scenarios. Table 8 lists the confuser shapes that pass the model fit metric; blank entries indicate a correctly identified shape. A confuser shape is crossed off the list with an orange '/' if it fails the RCS consistency check, that is, if it is not included in $\hat{C}_{m,n}$. A purple line is drawn through a confuser shape if it does not have the proper polarization bounce. We note that nearly all confusers are crossed off when combining the three metrics. The top-hat is confused with the dihedral in the monostatic SAR scenarios because the height dimension for the dihedral is inestimable in those cases, so the dihedral is not discarded on the basis of RCS inconsistency. The trihedral is confused with the plate in the bistatic SAR case because both shapes have sinc responses along their length and height and both are odd-bounce shapes. The plate, dihedral, cylinder, and sphere are correctly identified in the three scenarios presented in this paper. Alternate flight path choices will yield varying but similar results, as indicated by the scattering response plots of Figures 3 and 4. Overall, flight path diversity, peak scattering intensity calibration to radar cross section, and fully-polarimetric data improve identification of the canonical shapes.
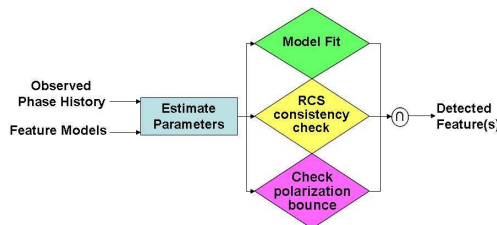

Figure 6. Feature classification algorithm

	Model Fit Errors (dB)					
True Signal	Plate	Dihedral	Trihedral	Cylinder	Top-hat	Sphere
Plate	-104.866	-104.176	-46.674	-103.404	-46.191	-46.191
Dihedral	-78.773	-78.722	-46.686	-81.544	-46.193	-46.193
Trihedral	-85.408	-85.473	-97.494	-91.162	-69.770	-64.529
Cylinder	-66.896	-70.566	-56.203	-70.631	-46.773	-46.776
Tophat	-63.321	-65.074	-64.325	-61.453	-65.208	-64.102
Sphere	-52.029	-73.951	-64.321	-74.008	-69.111	-74.304

Table 2. Model fit errors $\epsilon_{m,n}$ for monostatic SAR with the linear path depicted in Figure 3. Highlighted cells indicate target classes $\hat{F}_n$ with fits within $\tau_1 = 5$ dB of the best fit.

	Estimated Signal Radar Cross Section											
	Plate		Dihedral		Trihedral		Cylinder		Top-hat		Sphere	
True Signal	$\|S\|^2$	RCS	$\|S\|^2$	RCS	$\|S\|^2$	RCS	$\|S\|^2$	RCS	$\|S\|^2$	RCS	$\|S\|^2$	RCS
Plate	32.055	31.612	32.055	—	15.822	—	32.055	-48.734	8.228	—	7.437	-267.440
Dihedral	32.001	42.243	31.998	—	16.253	—	32.028	-4.588	8.233	—	7.454	-56.190
Trihedral	29.733	-254.789	29.733	—	29.938	—	29.773	-94.283	28.735	—	27.919	-135.249
Cylinder	6.600	-0.629	7.463	—	8.601	—	7.477	6.046	-8.182	—	-9.180	-12.963
Tophat	7.501	-34.266	8.105	—	8.376	—	7.833	-10.399	7.448	—	6.659	-13.168
Sphere	-6.900	-262.667	-6.717	—	-5.431	—	-6.742	-17.220	-6.152	—	-6.911	-6.936

Table 3. Estimated peak scattering intensity $\max \|S_m(\hat{\Theta}_{m,n})\|^2$ and estimated RCS computed from Table 1 for monostatic SAR with a linear flight path. Highlighted cells indicate $\hat{C}_{m,n}$ for an RCS match threshold of $\tau_2 = 5$ dB.

	Model Fit Errors (dB)					
True Signal	Plate	Dihedral	Trihedral	Cylinder	Top-hat	Sphere
Plate	-103.933	-62.307	-46.241	-60.784	-46.198	-46.196
Dihedral	-74.184	-74.088	-52.831	-73.622	-46.275	-46.263
Trihedral	-83.077	-84.886	-91.591	-82.865	-69.985	-64.232
Cylinder	-66.750	-70.464	-45.984	-70.375	-46.789	-46.772
Tophat	-61.649	-62.885	-62.200	-61.724	-65.362	-63.816
Sphere	-53.373	-59.841	-59.242	-58.847	-48.414	-72.495

Table 4. Model fit errors $\epsilon_{m,n}$ for monostatic SAR with the nonlinear flight path depicted in Figure 3. Highlighted cells indicate target classes $\hat{F}_n$ with fits within $\tau_1 = 5$ dB of the best fit.

	Estimated Signal Radar Cross Section											
	Plate		Dihedral		Trihedral		Cylinder		Top-hat		Sphere	
True Signal	$\|S\|^2$	RCS	$\|S\|^2$	RCS	$\|S\|^2$	RCS	$\|S\|^2$	RCS	$\|S\|^2$	RCS	$\|S\|^2$	RCS
Plate	32.058	32.063	31.463	—	9.247	—	31.221	-112.092	9.615	—	6.525	-267.676
Dihedral	32.049	19.098	32.033	—	33.697	—	31.976	13.550	11.797	—	8.194	-40.671
Trihedral	29.878	-22.209	29.933	—	29.988	—	29.883	-65.902	29.277	—	27.938	-99.649
Cylinder	6.597	-5.857	7.479	—	-9.773	—	7.482	6.694	-6.587	—	-9.222	-12.952
Tophat	8.007	-41.528	8.053	—	8.696	—	8.049	-28.471	8.152	—	6.723	-12.237
Sphere	-4.727	-3.482	-4.968	—	-4.961	—	-5.495	-41.429	-7.963	—	-6.935	-6.931

Table 5. Estimated peak scattering intensity $\max \|S_m(\hat{\Theta}_{m,n})\|^2$ and estimated RCS computed from Table 1 for monostatic SAR with an arbitrary, nonlinear flight path. Highlighted cells indicate $\hat{C}_{m,n}$ for an RCS match threshold of $\tau_2 = 5$ dB.

	Model Fit Errors (dB)					
True Signal	Plate	Dihedral	Trihedral	Cylinder	Top-hat	Sphere
Plate	-123.145	-86.828	-71.251	-69.832	-66.906	-46.600
Dihedral	-79.165	-78.741	-70.889	-68.995	-66.213	-46.943
Trihedral	-68.281	-68.093	-62.177	-65.770	-62.825	-47.796
Cylinder	-53.257	-70.311	-67.779	-70.090	-59.013	-49.120
Tophat	-63.171	-64.582	-61.607	-58.450	-64.698	-59.068
Sphere	-60.631	-68.737	-63.682	-62.020	-67.903	-70.799

Table 6. Model fit errors $\epsilon_{m,n}$ for the bistatic SAR nonlinear receiver flight path depicted in Figure 4. Highlighted cells indicate target classes $\hat{F}_n$ with fits within $\tau_1 = 5$ dB of the best fit.

	Estimated Signal Radar Cross Section											
	Plate		Dihedral		Trihedral		Cylinder		Top-hat		Sphere	
True Shape	$\|S\|^2$	RCS	$\|S\|^2$	RCS	$\|S\|^2$	RCS	$\|S\|^2$	RCS	$\|S\|^2$	RCS	$\|S\|^2$	RCS
Plate	32.043	32.058	32.041	33.065	31.925	35.471	31.595	-113.957	30.868	-117.711	13.197	-262.569
Dihedral	32.068	32.274	32.068	34.932	31.950	35.427	31.599	11.917	30.874	-32.922	14.705	-125.337
Trihedral	29.672	29.683	29.671	32.713	29.718	31.795	29.303	-9.127	28.449	-16.588	16.304	6.963
Cylinder	6.086	-4.913	7.564	12.945	7.741	24.691	7.478	6.634	5.029	29.100	-1.884	7.098
Tophat	7.047	-9.210	7.279	-5.370	8.215	12.016	7.178	-15.006	7.368	1.900	4.585	-12.716
Sphere	-6.821	-33.613	-6.566	-18.096	-4.951	2.581	-5.379	-41.658	-5.935	11.765	-6.927	-6.932

Table 7. Estimated peak scattering intensity $\max \|S_m(\hat{\Theta}_{m,n})\|^2$ and estimated RCS computed from Table 1 for bistatic SAR with a fixed transmitter and arbitrary, nonlinear receiver flight path. Highlighted cells indicate $\hat{C}_{m,n}$ for an RCS match threshold of $\tau_2 = 5$ dB.

	Best-fit Confuser Shapes		
True Shape	Monostatic Linear	Monostatic Nonlinear	Bistatic Nonlinear
Plate	~~dihedral~~ cylinder		
Dihedral	plate cylinder	plate cylinder	plate
Trihedral			plate, ~~dih~~, cyl, top-hat
Cylinder	plate dihedral	plate dihedral	~~dihedral~~ trihedral
Top-hat	plate, dih, ~~trih~~, cyl, sphere	plate, dih,~~trih~~, cyl, sphere	plate, dihedral, ~~trihedral~~
Sphere	~~dihedral~~ cylinder		~~dihedral, top-hat~~

Table 8. Summary of feature identifiability. Confuser shapes are listed for the model fit discriminator and are crossed off with an orange '/' if they do not pass the RCS consistency check and with a purple line if they do not have the proper polarization bounce.

4. CONCLUSION

We have considered the identifiability of feature parameters that describe six canonical scattering shapes. We have specifically considered three sparse aperture cases: a monostatic linear aperture, a monostatic nonlinear aperture with both azimuth and elevation diversity, and a bistatic nonlinear aperture. We have demonstrated that, using the anisotropic scattering response shape alone, it is often not possible to distinguish between some canonical shapes from these sparse apertures. When polarization properties and uncertain radar amplitude calibration are used in addition to anisotropic shape, many fewer canonical shapes are confused. The results specify exactly which shapes may be confused with which other shapes under the various apertures and for the various polarimetric or amplitude information cases considered.

The fact that shapes are not always uniquely identifiable does not detract from the usefulness of scattering primitive models. In fact, the use of canonical shapes for higher-level reasoning about target and scene composition is a considerable advantage. On the other hand, it is important to identify and quantify the possible uncertainties that remain from single-aperture identification of scattering features, so that the higher-level reasoning process is aware of the possible ambiguities and is provided with the list of possible canonical shapes that are consistent with the measured data from each single aperture. By combining this information with other apertures or by comparing against a limited set of possible targets, this feature uncertainty can be propagated to uncertainty in higher-level inference outputs.

REFERENCES

1. L. C. Potter and R. L. Moses, "Attributed scattering centers for SAR ATR," in *IEEE Transactions on Image Processing*, **6**(1), pp. 79–91, January 1997.
2. M. Gerry, *Two-Dimensional Inverse Scattering Based on the GTD Model*, Ph.D. Disseration, The Ohio State University, 1997.
3. M. Koets, *Automated Algorithms for Extraction of Physically Relevant Features from Synthetic Aperture Radar Imagery*, M.S. Thesis, The Ohio State University, 1998.
4. B. Rigling, *Signal Processing Strategies for Bistatic Synthetic Aperture Radar*, Ph.D. Dissertation, The Ohio State University, 2003.
5. J. A. Jackson and R. L. Moses, "Feature extraction algorithm for 3D scene modeling and visualization using monostatic SAR," in *Algorithms for Synthetic Aperture Radar Imagery XIII*, E. G. Zelnio and F. D. Garber, eds., *Proceedings of SPIE* **6237**, 2006.
6. J. R. Huynen, "Phenomenological theory of radar targets," in *Electromagnetic Scattering*, P. L. E. Uslenghi, ed., Academic Press, (New York), 1978.
7. J. A. Richards, A. S. Willsky, and J. W. Fisher III, "Expectation-maximization approach to target model generation from multiple synthetic aperture radar images," in *Optical Engineering*, D. C. O'Shea, ed., **41**(01), pp. 150–166, 2002.
8. W. L. Cameron and L. K. Leung, "Feature motivated polarization scattering matrix decomposition," in *IEEE International Radar Conference*, pp. 549–557, 1990.
9. R. Dilsavor, *Detection of Target Scattering Centers in Terrain Clutter Using an Ultra-Wideband, Fully-Polarimetric Synthetic Aperture Radar*, Ph.D. Dissertation, The Ohio State University, 1993.
10. E. Ertin, *Polarimetric Processing and Sequential Detection for Automatic Target Recognition Systems*, Ph.D. Dissertation, The Ohio State University, 1999.
11. B. D. Rigling and R. L. Moses, "GTD-based scattering models for bistatic SAR," in *Algorithms for Synthetic Aperture Radar Imagery XI*, E. G. Zelnio, ed., *Proceedings of SPIE* **5427**, pp. 208–219, 2004.
12. "Xpatch version 4.7.16," SAIC Demaco, 2002.
13. G. T. Ruck, ed., *Radar Cross Section Handbook*, Plenum Press, New York, 1970.
14. E. F. Knott, J. F. Shaeffer, and M. T. Tuley, *Radar Cross Section, Second Edition*, Artech House, Boston, 1993.